Quadrupolar excitation channels at the L_3 edge of rare-earth ions probed by resonant inelastic x-ray scattering

Fernando Bartolomé
Laboratoire de Cristallographie, CNRS, Boîte Postale 166, 38042 Grenoble, France
and Instituto de Ciencia de Materiales de Aragón, C.S.I.C., Universidad de Zaragoza, 50009 Zaragoza, Spain

Michael H. Krisch
European Synchrotron Radiation Facility, Boîte Postale 220, 38043 Grenoble Cedex, France

Denis Raoux and Jean-Marc Tonnerre
Laboratoire de Cristallographie, CNRS, Boîte Postale 166, 38042 Grenoble Cedex, France
(Received 6 April 1999; revised manuscript received 14 June 1999)

A systematic resonant inelastic x-ray scattering study at the L_3 absorption edge of rare-earth ions in the $R_2Fe_{14}B$ intermetallics is presented. The energy position and the relative strength of quadrupolar ($E2$) and dipolar ($E1$) intermediate-state excitation channels are extracted by decomposing the inelastic scattering spectra into their main contributions. For the cases in which theoretical calculations of the quadrupolar part are available, a good agreement for the spectral shape is found. With increasing atomic number, a monotonic increase of the energy difference and a decrease of the relative strength between $E1$ and $E2$ excitation channels is observed. This work provides important experimental data for the application of magneto-optical sum rules to the $5d$ band of rare-earth systems, as well as for the validation of theoretical models aimed at a correct description of x-ray magnetic spectroscopies at the L edges of rare earths in metallic systems. [S0163-1829(99)00440-3]

I. INTRODUCTION

The interpretation of x-ray magnetic circular dichroism (XMCD) and x-ray resonant magnetic scattering (XRMS) recorded at the $L_{2,3}$ absorption edges of rare-earth (RE) ions has been a matter of debate since the first experimental results were obtained.[1–4] The spectra, dominated by the strong dipolar $2p \rightarrow 5d$ electronic transition, are not straightforwardly connected to the spin polarization of the rare-earth $5d$ band. Several aspects have to be included in a correct description of the experiments, such as the contribution from quadrupolar excitation channels in the pre-edge region,[5] the intra-atomic $4f$-$5d$ exchange interaction;[6] and the spin dependence of the radial matrix elements.[6,7] The first of these aspects, namely, the quadrupolar nature ($2p \rightarrow 4f$ transitions) of the pre-edge structures, has been well established in the last few years by several experimental techniques[8–17] and calculations.[18–21] Despite their weak absorption intensities, these quadrupolar excitations give rise to strong dichroic signals at the L edges of rare-earth ions, as they access the $4f$ shell, which is the magnetic moment carrier of the rare-earth ion. The determination of the energy position and the relative strength of the $E2$ and $E1$ excitation channels is therefore essential, not only to provide relevant information for the correct interpretation of XMCD data of RE compounds, but also to test and refine existing calculations, aiming at a complete understanding of rare-earth magnetism.

In a previous publication,[17] we presented the preliminary results of a resonant inelastic x-ray scattering (RIXS) study at the L_3 absorption edge of rare-earth ions in the intermetallic series $R_2Fe_{14}B$ (R=Nd, Sm, and Gd to Tm). Weak resonances, ascribed to $2p \rightarrow 4f$ quadrupolar excitations, were systematically observed at energies below the L_3 white-line. The results evidenced the necessity of their inclusion for a correct interpretation of XMCD and XRMS experiments recorded at the L edges of rare-earth systems.

In this paper, we present the whole set of experimental results (completed with RIXS data recorded at the Yb L_3 edge in $Yb_2Fe_{14}B$). The data analysis is based on a decomposition of each inelastic scattering spectrum into its main final-state multiplet families. These multiplet families arise from the decay of dipolar or quadrupolar intermediate state excitation channels, which are resonantly enhanced as the incident photon energy is tuned through the absorption edge. The decomposition procedure allows a determination of the excitation energies and the relative strength of each absorption channel. The paper is organized as follows: Sec. II provides the theoretical background. The general characteristics of the RIXS cross section are illustrated by experimental results obtained at the Yb L_3 edge in $Yb_2Fe_{14}B$. Section III describes the experimental setup. In Sec. IV the experimental spectra are presented, followed by a detailed description of the analysis procedure. The extracted spectral shape for the final state multiplet arising from $2p \rightarrow 4f$ $E2$ transitions is compared to theoretical results, whenever they are available. Finally, the quantitative results concerning the energy position and the relative strength of $E1$ and $E2$ excitations are discussed. The conclusions of the paper are presented in Sec. V.

II. RIXS PROCESS

The cross section for resonant inelastic x-ray scattering is given by the Kramers-Heisenberg formula,[22–25] and the in-

elastically scattered intensity observed within a solid angle Ω and a scattered energy intervall $\Delta\hbar\omega'$ can be written as[20]

$$I \propto \sum_f \left| \sum_m \frac{\langle f|H_{int}|m\rangle\langle m|H_{int}|i\rangle}{\hbar\omega + E_i - E_m + i\frac{\Gamma_m}{2}} \right|^2 \times \delta(\hbar\omega - \hbar\omega' + E_i - E_f), \quad (1)$$

where $\hbar\omega$ and $\hbar\omega'$ are the energies of the incident and the scattered photon, E_i, E_m, and E_f are the energies of the initial, intermediate and final states, Γ_m is the lifetime broadening of the intermediate state, and $H_{int}=(e/2m)(\mathbf{pA}+\mathbf{Ap})$ is the interaction Hamiltonian which is usually expanded in electric 2^L-pole transition operators. In a simple one-electron picture, RIXS is interpreted as an ''absorption followed by emission'' process. In the first step a photon of energy $\hbar\omega$ is absorbed by exciting a core electron into an empty state, leading to the intermediate-state electronic configuration $|m\rangle$. In the second step the deep core hole, created in the absorption step, is filled up by an electron from a shallower core level or the valence band under emission of a photon of energy $\hbar\omega'$. In order to account for the lifetime broadening in the final state of the scattering process, the δ function has to be replaced by a Lorentzian of width Γ_f. Moreover, the experimental spectra are smeared out by the resolution function. For incident photon energies well above the absorption threshold, the electron is promoted into continuum states, and the emission is identified as fluorescence whose width (in absence of strong multiplet effects) is given by approximately $\Gamma_m+\Gamma_f$. For $\hbar\omega$ in the vicinity or below the absorption threshold, the behavior is more complex. In particular in open-shell systems, such as transition metals and rare earths, a simple one-electron picture is not sufficient to account for all the observed phenomena, and a many-body description has to be invoked. The Coulomb and exchange interactions between the electrons of the two incomplete shells in the intermediate and final states can lead to distinct multiplet families which might extend over several eV. In these cases, the inelastic x-ray spectra are ultimately only limited by Γ_f, whereas Γ_m is merely responsible for the intensity variation of the features as the incident photon energy is varied. In cases where the sudden approximation is fulfilled, the integrated intensity of the inelastic x-ray scattering spectrum, recorded at a specific incident energy, is proportional to the absorption cross section at this energy.[31] A successful decomposition of the RIXS spectra into quadrupolar and dipolar contributions should therefore provide the partial $E1$ and $E2$ absorption cross sections, if interference effects can be neglected. Experimentally, the RIXS intensity is measured within the zone of interest of the $(\hbar\omega,\hbar\omega')$ plane by scanning the scattered photon energy $\hbar\omega'$ at different fixed incident photon energies $\hbar\omega$ around the absorption edge (IXS scans). Alternatively, the intensity evolution of a specific final-state multiplet family can be studied by scanning the incident and scattered photon energy together, thus keeping the energy transfer $\hbar\omega-\hbar\omega'$ constant and fixed to values corresponding to the excitation energies of this multiplet family [constant final-state (CFS) scans].

In order to illustrate the main characteristics of the RIXS cross section, and to clarify the presentation of the experimental results given in the following sections, we present an overview of the observed structures and theoretical assignments which are common to the RIXS spectra of all our studied samples, exemplified by the results obtained at the Yb L_3 edge of $Yb_2Fe_{14}B$. Due to its $4f^{13}5d^{\tilde{n}}$ ground-state electronic configuration, with only one hole in the $4f$ shell, the intermediate- and final-state multiplets are composed of only a few lines, closely grouped, leading to the structureless shape of the $E2$ Yb RIXS features. The occupation number of the rare-earth $5d$ shell in the ground-state electronic configuration has been denoted by $\tilde{n}$. For selected rare-earth ions, theoretical values of $\tilde{n}$ for each crystallographic position have been determined by band-structure calculations [for example, $\tilde{n}\approx 1.8$ for Nd in $Nd_2Fe_{14}B$ (Ref. 26)]. Panel (a) of Fig. 1 shows a three-dimensional plot ($\hbar\omega$, $\hbar\omega'$, intensity) of some representative IXS spectra recorded at various incident photon energies around the Yb L_3 edge, obtained by monitoring the $3d_{5/2}\rightarrow 2p_{3/2}$ radiative decay channel ($L\alpha_1$ fluoresence well above threshold). Panel (b) is an enlargement of the low-$\hbar\omega$–high-$\hbar\omega'$ zone of panel (a). The intensity scale on both panels refers to the same (arbitrary) units. For clarity, some of the high incident energy RIXS spectra have been removed from panel (b) and others have been added. From panels (a) and (b), three distinct features, labeled *A*, *B*, and *C*, can be identified. Their scattered energy $\hbar\omega'$ is depicted as a function of incident photon energy $\hbar\omega$ in panel (c). Below the absorption edge, features *A* and *B* display the usual Raman shift, i.e. as the incident photon energy increases, the emitted energy at which a specific feature is observed increases by the same amount. Above $\hbar\omega=8948.5$ eV, corresponding roughly to the white-line maximum, feature *C* is observed at the fixed scattering energy of 7416 eV, with an approximately constant intensity. In contrast to this, features *A* and *B* do not settle at a fixed $\hbar\omega'$ value, but continuously disperse, and both display a Lorentzian intensity variation as a function of $\hbar\omega$ with a maximum at 8936.6 eV (feature *A*, $\hbar\omega'=7416.6$ eV, $\hbar\omega-\hbar\omega'=1520$ eV) and 8948.5 eV (feature *B*, $\hbar\omega'=7416.0$ eV, $\hbar\omega-\hbar\omega'=1531.3$ eV). Furthermore, we note that feature *A* is about a factor 40 weaker than feature *B*.

Feature *C* is identified as the $L\alpha_1$ fluorescence, corresponding to $3d^9 4f^{13}5d^{\tilde{n}}\epsilon^*$ final states, arising from $2p^5 4f^{13}5d^{\tilde{n}}\epsilon^*$ intermediate states in which the $2p$ core hole is promoted into empty continuum states of *d* symmetry. The fluorescence is observed at about the energy difference between the M_5 and L_3 binding energies. The extra energy available, amounting to $\hbar(\omega-\omega')-E_{L\alpha_1}$, is transferred to the photoelectron as kinetic energy. Features *A* and *B* show the typical behavior of a transition in which the photoelectron is promoted into a discrete state, thus acquiring no kinetic energy [note the slope equal to 1 of *A* and *B* branches in panel (c) of Fig. 1]. In this case, the expression $\hbar\omega+E_i-E_m$ is zero only at the exact energy necessary to promote the electron into this specific state. As a consequence of energy conservation, the corresponding feature in the IXS spectrum is always observed at a fixed energy transfer $\Delta E=\hbar\omega-\hbar\omega'$ for all $\hbar\omega$, while the resonant denominator in Eq. (1) is responsible for the observed Lorentzian intensity variation.

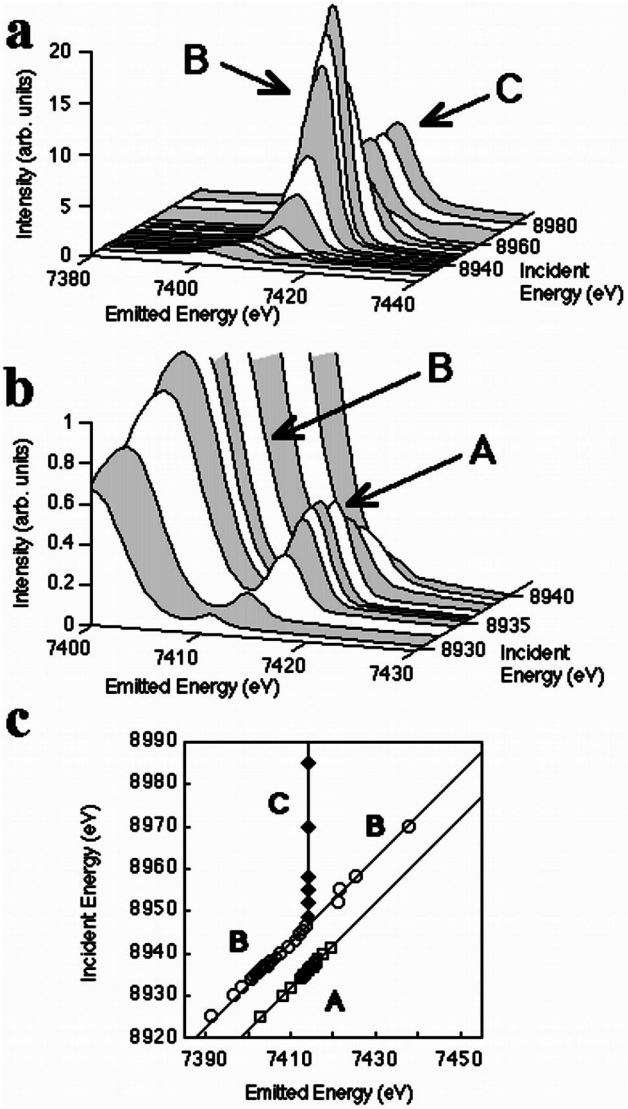

FIG. 1. Panels (a) and (b) show representative IXS scans recorded at the Yb L_3 edge of the $Yb_2Fe_{14}B$, by monitoring the $3d_{5/2}\rightarrow 2p_{3/2}$ radiative decay channel. Three groups of features, labeled *A*, *B*, and *C*, can be identified. Feature A is much weaker than features *B* and *C*, and is therefore shown on a reduced scale, focused on the low-incident-energy part of the surface, in panel (b). Panel (c) shows the energy positions in the $(\hbar\omega,\hbar\omega')$ plane of the different maxima observed in the recorded IXS scans.

Feature *B* is ascribed to the localized $3d^9 4f^{13} 5d^{\tilde{n}+1}$ final-state multiplet, resonantly enhanced at the $2p^5 4f^{13} 5d^{\tilde{n}+1}$ intermediate state excitation energy, corresponding to the dipolar $2p\rightarrow 5d$ channel. The much weaker feature *A* is assigned to the $3d^9 4f^{14} 5d^{\tilde{n}}$ final state which is resonantly enhanced at the $2p^5 4f^{14} 5d^{\tilde{n}}$ intermediate-state excitation energy, corresponding to the quadrupolar $2p\rightarrow 4f$ excitation channel. In both cases the intermediate state is a result of excitations into localized states. Although RIXS does not allow a direct multipolar assignment of the observed features, sufficient experimental and theoretical evidence is available to support our assignment, besides simple qualitative arguments: Feature *A* is observed at a lower-energy transfer than feature *B*, i.e., at smaller intermediate state excitation energies. This is consistent with the strength of the Coulomb interaction between the promoted electron and the $3d$ core-hole resulting in a $3d^9 4f^{14} 5d^{\tilde{n}}$ final state more strongly bound than the localized $3d^9 4f^{13} 5d^{\tilde{n}+1}$ (*B*) or the delocalized $3d^9 4f^{13} 5d^{\tilde{n}} \epsilon *$ state (*C*).

As will be shown in Sec. IV, the RIXS spectra of all the other compounds from Nd through Tm show the same characteristics. The final state multiplet arising from $2p\rightarrow 4f$ intermediate-state excitations displays a richer structure as a consequence of the more or less filled $4f$ shell with $4f^{n+1}$ varying from $4f^4$ (for Nd) to $4f^{13}$ (for Tm).

TABLE I. Emission lines, absorption L_3-edge energies, and analyzer reflection used on each $R_2Fe_{14}B$ system.

R ion	L_3 edge (eV)	Emission line (eV) $L\alpha_1$ $3d_{5/2}\rightarrow 2p_{3/2}$	Emission line (eV) $L\beta_{2,15}$ $4d_{3/2,5/2}\rightarrow 2p_{3/2}$	Analyzer Si (*hkl*)
Nd	6208		6089	(333)
Sm	6716		7178	(440)
Gd	7243	6057		(333)
Tb	7514	6273		(333)
Dy	7790	6495		(440)
Ho	8071	6720		(440)
Er	8358		6189	(444)
Tm	8648	7180		(531)
Yb	8944	7416		(620)

III. EXPERIMENTAL DETAILS

The experiments were performed on the beamlines ID16 at the European Synchrotron Radiation Facility[27] (for Sm through Yb) and X21 at the National Synchrotron Light Source[28] (for Nd). At ID16, a Si(111) monochromator provided a 0.5 (horizontal) $\times$1.5 (vertical) mm^2 beam. At X21, a dispersive four-bounce Si(220) crystal setup in conjunction with a toroidal mirror provided a 0.5×0.5-mm^2 beam. In both cases, the incident beam was linearly polarized in the horizontal plane. The scattered radiation was analyzed by a 1-m spherical crystal spectrometer in Rowland geometry, at 90° scattering angle in the horizontal plane in order to minimize the contribution from nonresonant Thomson and inelastic scattering. The choice of either the $3d_{5/2}\rightarrow 2p_{3/2}$ ($L\alpha_1$) or $4d_{5/2,3/2}\rightarrow 2p_{3/2}$ ($L\beta_{2,15}$) deexcitation channel was driven by the availability of a convenient crystal analyzer reflection, providing Bragg angles between 65° and 85° in order to comply with the geometrical constraints of the experimental setup. This implied slight differences in the energy resolution achieved for different samples. The overall experimental resolution was better than 1-eV full width at half maximum (FWHM) at X21 and within the range of 1–1.5 eV FWHM at ID16. The emission lines and absorption edge energies around which the experiments were performed are presented in Table I, together with the utilized analyzer reflection. The rare-earth alloys were prepared by arc melting the starting elements in Ar atmosphere. A more detailed description of its preparation and characterization is given elsewhere.[29] Powdered samples of about 2-mm thickness sealed in kapton tape were used in the inelastic scattering experiments. Transmission absorption spectra obtained on thin samples were

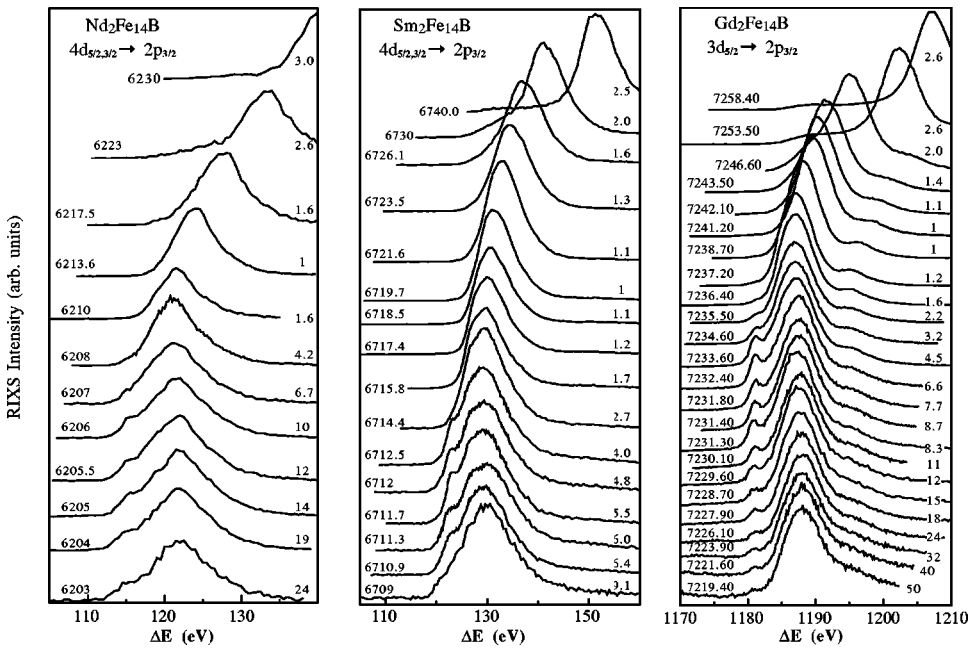

FIG. 2. Resonant inelastic x-ray scattering spectra measured in $R_2Fe_{14}B$ for light rare earths (R=Nd, Sm, and Gd) as a function of energy transfer, ΔE. For the sake of clarity, the spectra have been scaled to the same maximum height, by a factor displayed on the right side of each curve. The incident photon energy at which the IXS spectrum has been recorded is indicated on the left side of each curve.

recorded and scaled to absolute values using tabulated values for the photoelectric absorption coefficient μ, well below and above the absorption threshold. The absorption spectra obtained in this way were used to correct the IXS spectrum for self-absorption effects.

IV. RESULTS AND DISCUSSION

A. Experimental RIXS spectra

The whole set of experimental spectra obtained in the $R_2Fe_{14}B$ series is shown in Figs. 2 (R=Nd, Sm, Gd) and 3 (R=Tb, Dy, Ho, Er, Tm, Yb). The spectra are presented as a function of energy transfer $\Delta E=\hbar(\omega-\omega')$, instead of scattered energy. In this way, features A and B (i.e., those originating from transitions into localized states) remain at a constant position as the incident photon energy is tuned through the edge. In contrast to this, feature C (appearing in the high-incident-energy curves on top of each panel) moves toward higher ΔE values as the incident energy increases above threshold. The incident photon energy at which the IXS spectrum has been recorded is indicated at the left side of each curve. In order to render the whole series of data visible in a single picture, the spectra have been normalized to the same maximum height. The applied scaling factors are displayed at the right side of each spectrum.

The spectra for all compounds show some common features and systematics, with the same assignments as for the case of Yb. The dominating features correspond to $\mathbf{n}d^9 4f^n 5\tilde{d}^{n+1}$ final states, not dispersing in ΔE, and $\mathbf{n}d^9 4f^n 5\tilde{d}^n \epsilon^*$ final states, constituting the $L\alpha_1$ ($\mathbf{n}$=3) or $L\beta_{2,15}$ ($\mathbf{n}$=4) fluorescence, observed at increasing ΔE (fixed scattered energy). The shape of these fluorescence lines, in particular toward larger energy transfers, is different for each rare-earth compound, since it is controlled by the electrostatic and exchange interactions between the $3d$ ($4d$) and $4f$ electronic shells. This in turn strongly depends on the occupancy of the $4f$ shell and the principal quantum number $\mathbf{n}$ of the final state core hole. The multiplet of type $\mathbf{n}d^9 4f^{n+1} 5\tilde{d}^n$, arising from quadrupolar $2p \rightarrow 4f$ intermediate-state excitations, appears at the low-energy-transfer side. While in light rare earths they do not appear very pronounced, they become more distinct as one continues in the R series. In particular for $Dy_2Fe_{14}B$ and $Tm_2Fe_{14}B$, the multiplet is spread over a few eV, and is composed of more than one line. Moreover, one can observe that the energy separation between the $E2$ and $E1$ multiplets increases with increasing atomic number Z.

The energy width of the $E1$ RIXS feature in metallic systems is larger than that found in insulators, since it is directly related to the width of the rare-earth $5d$ band. This makes the details of feature A hard to observe in a metallic system. For example, the quadrupolar double structure calculated for Gd,[31,32] which was observed[15] at the Gd L_3 edge in $Gd_3Ga_5O_{12}$, cannot be identified by eye inspection in our RIXS experiment on $Gd_2Fe_{14}B$, nor in that performed on a pure Gd metal[16] foil. However, the data analysis procedure presented in Sec. IV B reveals a remnant of such a structure even in our data (see Fig. 5).

To investigate the evolution of the intensities of the two multiplets A and B as a function of incident photon energy, we recorded scans at constant energy transfer, corresponding to the excitation energy of the A and B final-state multiplets. These (CFS) scans are a direct way to find the excitation energy of a given transition from the ground to the intermediate state. However, the intensity due to quadrupolar excitations can not be correctly determined, because the CFS scans corresponding to quadrupolar transitions usually lie on the dipolar tail of the dominating $E1$ multiplet. A correct determination of $E1$ and $E2$ intensities therefore requires a proper decomposition of the experimental spectra. This has been attempted by describing the experimental RIXS spectra as a sum of phenomenological profiles. The fitting procedure of the experimental curves is described in detail in Sec. IV B.

B. Fitting procedure and results

For each R ion, the first step is to fit the profile of the fluorescence line recorded at the highest incident energy. In

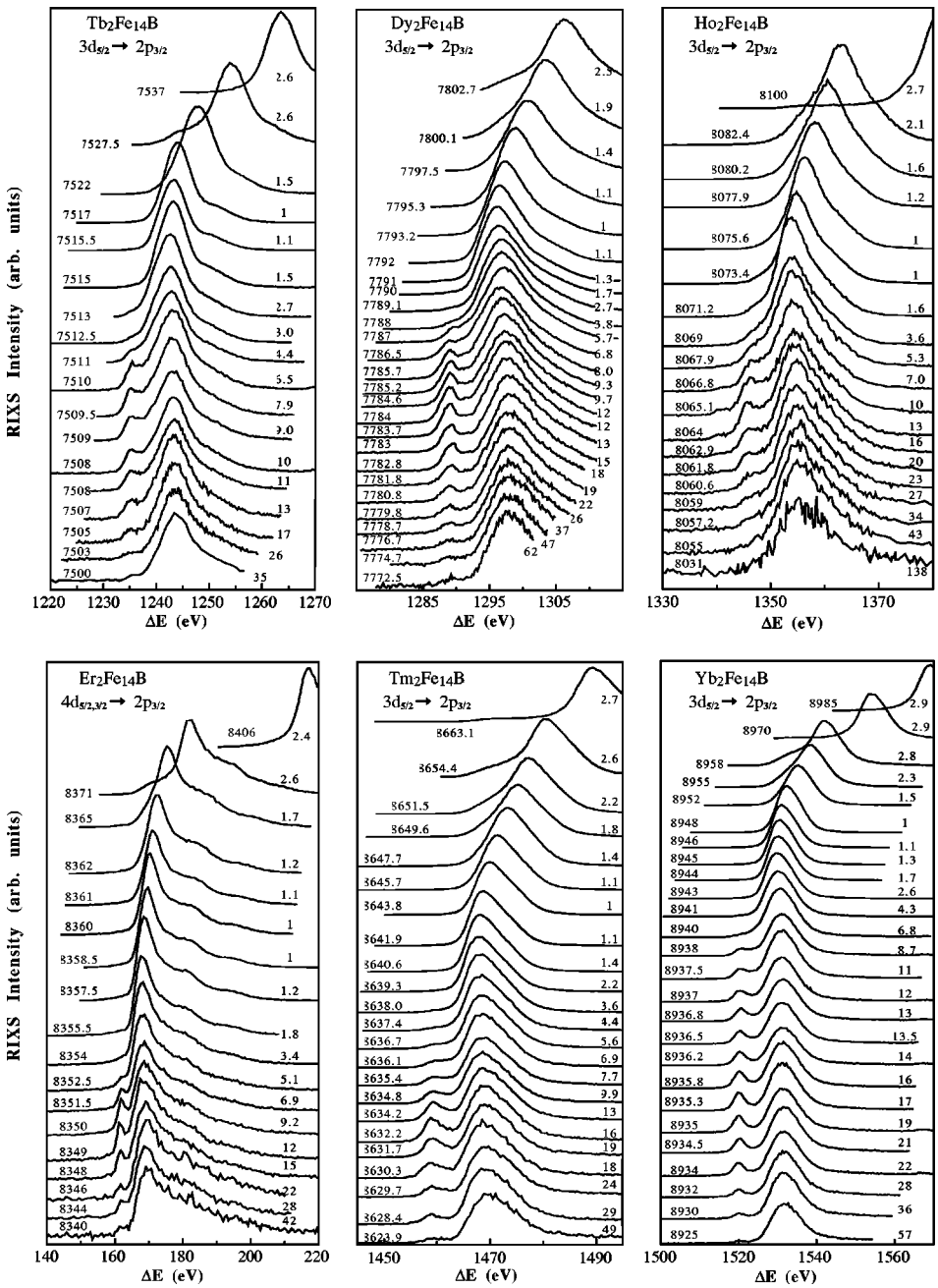

FIG. 3. Resonant inelastic x-ray scattering spectra measured in $R_2Fe_{14}B$ for heavy rare earths (R=Tb, Dy, Ho, Er, Tm, and Yb) as a function of energy transfer, ΔE. For the sake of clarity, the spectra have been scaled to the same maximum height, by a factor displayed on the right side of each curve. The incident photon energy at which the IXS spectrum has been recorded is indicated on the left side of each curve.

general, a sum of two pseudovoigt profiles is the minimal functional assumption which allows a proper reproduction of the asymmetric shape of the fluorescence line with a minimum number of parameters. This is a fully phenomenological approach, and no theoretical considerations have been taken into account when obtaining this fitted profile. As an example, in Fig. 4 we show the analysis performed for $Dy_2Fe_{14}B$. Panel (a) shows the experimental ($\bigcirc$) and the fitted profile (full line) of the Dy $L\alpha_1$ line at $\hbar\omega$ =7823 eV, 33 eV above the absorption edge. The fitted profile is the sum of two pseudo-Voigt peaks, indicated by dashed lines. The resulting fitted profile is then used to fit the other RIXS spectra in the high-energy region above the threshold with the constraints that the intensities and widths of each pseudo-Voigt peak are not allowed to change independently. All the spectra recorded at $\hbar\omega$ within this high-incident-energy region can be successfully fitted by displacing the energy position of the fluorescence profile by $7823-\hbar\omega$ and adjusting the intensity of the profile.

As $\hbar\omega$ approaches the absorption edge energy, feature B starts to contribute in the low-energy-transfer part of the spectrum (at a constant ΔE value). In such a case, the spectra have been fitted by two groups of profiles with the same shape determined previously from the $L\alpha_1$ fluoresence: one centered at fixed scattered energy, corresponding to feature C, and one at fixed energy transfer, corresponding to feature B. The choice of the same shape for features B and C can be justified by the fact that the respective multiplets only differ by the occupancy of the $5d$ shell. Panel (b) in Fig. 4 shows the Dy RIXS spectra for $\hbar\omega$=7802.7 eV. The full line is the sum of the two described contributions, shown as dashed lines.

The spectra excited with incident photon energies around the whiteline maximum are slightly narrower whereas the

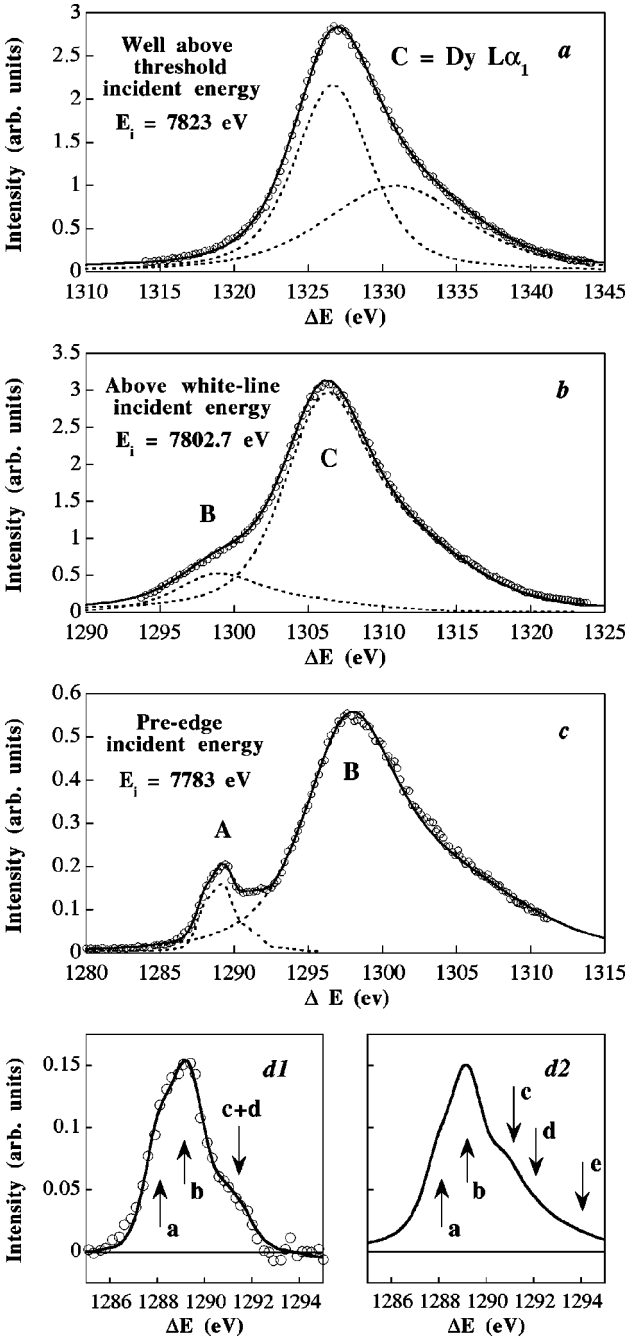

FIG. 4. Illustration of the fit and decomposition procedure for the Dy RIXS spectra. The open circles denote the experimental data, the solid line the best fit, and the dashed lines the individual components of the fit. For excitation energies well above threshold [panel (a)] two pseudo-Voigt profiles are used to account for the asymmetric shape of the line. Panel (b) shows the best fit for a spectrum recorded slightly above the whiteline energy. In this case two groups of functions of the same shape as the fluorescence line in panel (a) are utilized. Panel (c) shows the best fit for a spectrum recorded in the pre-edge region. The shape of the quadrupolar feature A is obtained by subtraction of the dipolar part. Panel (d1) shows the experimental quadrupolar contribution, and a fit utilizing four Lorentzian functions, in comparison with the theoretical one [panel (d2) and Ref. 19]. The different contributions to this multiplet family which can be identified are labeled *a*, *b*, *c*, and *d*. For further details see text.

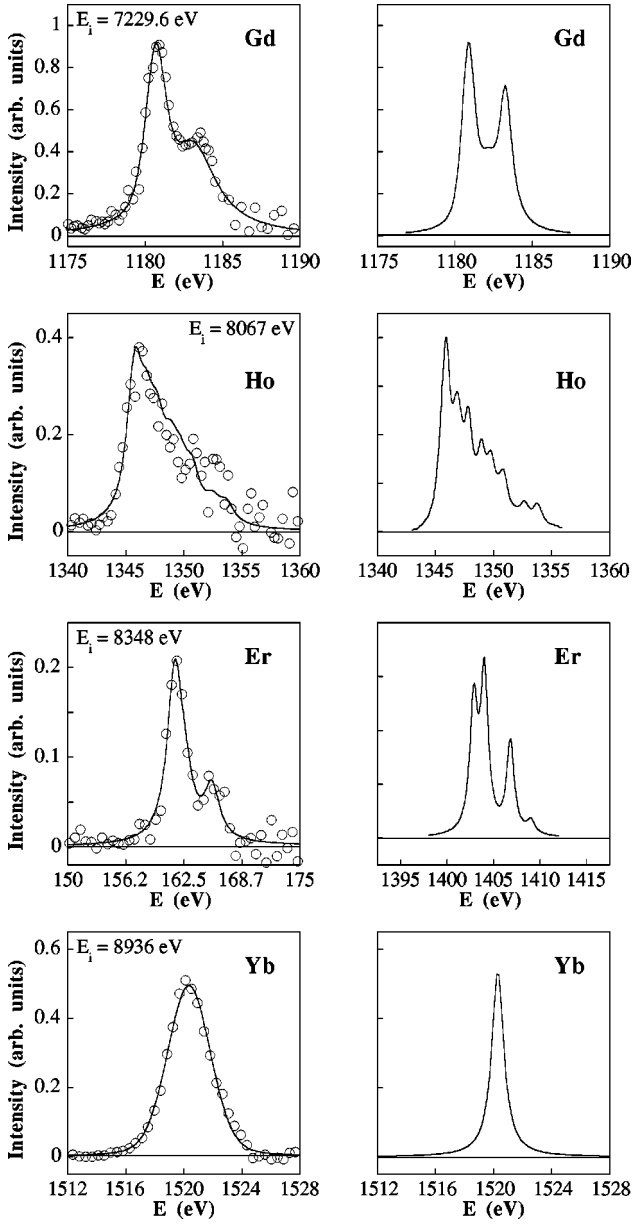

FIG. 5. Comparison between the experimental quadrupolar contributions (right panels, ○) in several $R_2Fe_{14}B$ systems (R=Gd, Ho, Er, and Yb) and the corresponding ones for Gd, Ho, and Er (left panels), calculated in the pre-edge region as available from literature (Ref. 31). The Yb calculated curve is a single Lorentzian. The lines shown in the left panels have been obtained by fitting the experimental data with pseudo-Voigt profiles at positions given by theory. For further details, see text.

spectra below the absorption threshold display an increasing width. This is the well-known behavior in the so-called resonant Raman regime. It is easily derived by inspection of the resonant denominator in Eq. (1) and energy conservation considerations. The initially determined fluorescence profile satisfactorily reproduces the observed shape of feature *B*, when recorded at low incident energies just by slightly enlarging its width (by at most 15%). This is illustrated in panel (c) of Fig. 4. The quadrupolar contribution can thus be extracted by subtracting the fitted dipolar contribution. The result of this procedure is shown in panel (d1) of Fig. 4, where the quadrupolar part of the experimental data is shown

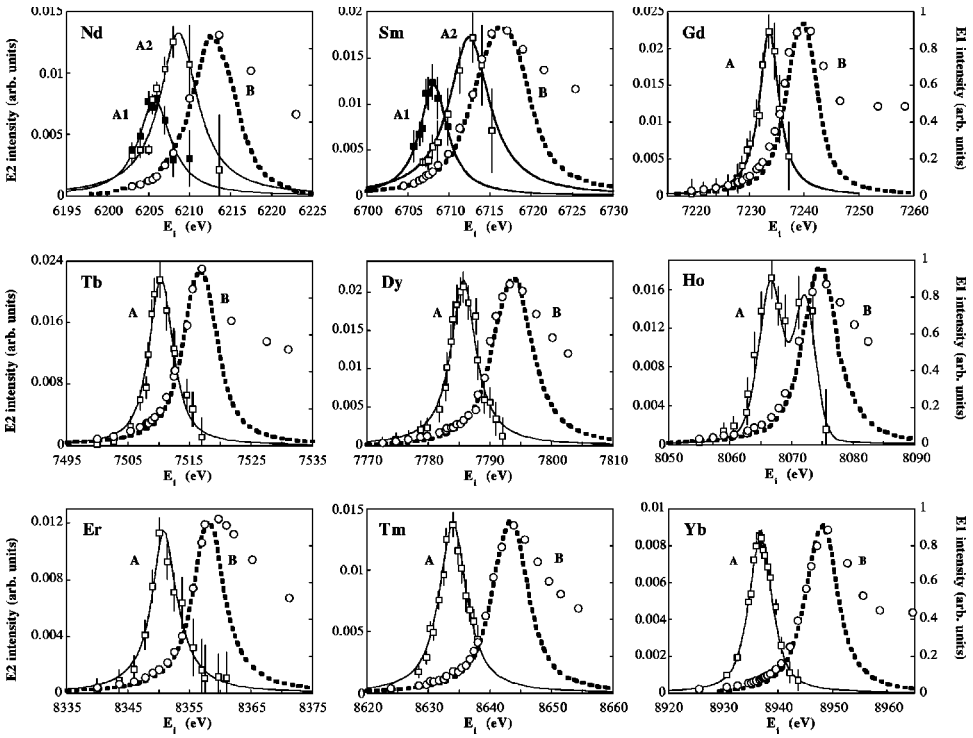

FIG. 6. Dipolar (○, right scale) and quadrupolar (□, left scale) intensities obtained from the analysis described in the text. Each figure has been scaled to have a dipolar maximum of 1 (for the sake of clarity it is only shown in the left panels). The scales of the quadrupolar intensities are in the same units, and are shown on the left side of each panel. The experimental CFS scans recorded at energy transfer corresponding to dipolar excitations (dashed lines) have been scaled in order to have the same maximum. Profiles fitting the quadrupolar intensities are shown as a guide to the eye (continuous lines).

as open circles. For the Dy^{3+} ion, the quadrupolar contribution has been previously calculated[19,25,31] and the energies of several quadrupolar contributions have been predicted. In panel (d2) of Fig. 4, we show the calculated curve from Ref. 19 (which is essentially the same as those calculated by other authors[25,31]) for an incident energy close to that of the experimental data shown in panel (d1). The arrows indicate the energy positions of the predicted quadrupolar contributions. The agreement between the calculated and experimental curves is rather good. It is important to note that this qualitative agreement with the calculated $E2$ part gives convincing evidence for the $E2$ nature of the observed pre-edge absorption channels, even though RIXS itself does not allow a direct multipolar assignment of a given spectral feature. Such an agreement allows inclusion in the fitting procedure of several quadrupolar contributions to describe the observed signal. The positions are fixed by the theory, and the width is fixed to the experimental resolution value. However, to reduce the number of free parameters, we have allowed for three peaks instead of five: features *c* and *d* of the calculated profile are too close to be resolved by our experiment and have been merged into one; feature *e* has not been included as it appears too high in energy transfer to be separated from the dipolar main line. The resulting fit is shown as a solid line in panel (d1), and as dashed line as well in panel (c).

For Ho, Gd, and Er, theoretical calculations of the $E2$ part of the RIXS signal are as well available,[31] and a general agreement between theory and experiment is found, as shown in Fig. 5. For these three rare earths we show the experimental quadrupolar multiplet (left panels, ○), extracted as described above for Dy, together with the calculations performed by van Veenendaal *et al.*[31] in the pre-edge region (right panels). The calculated curves cannot be directly compared to our experimental results: first, the incident photon energies of both do not match exactly, and second, the theoretical curves were calculated with an overall width of $\Gamma = 0.5$ eV, which is significantly smaller than the experimental resolution. However, by using the same procedure described for Dy, it is possible to fit the $E2$ contribution extracted from the experimental data with a combination of contributions at fixed positions given by theory. This leads to the curves shown with the experimental data in the left panels in Fig. 5. The overall agreement is very good, though the experimental curves are broader ($\Gamma_{expt} \geqslant 1$ eV), and very closely lying theoretical structures merge together. Moreover, the observed profiles are more Voigt-like than pure Lorentzian ones as a result of the convolution of the experimental and lifetime induced broadenings. To further stress this point, we include the Yb data, where the $E2$ contribution is composed of a single line due to its $4f^{13}$ electronic ground-state configuration. In analogy to the other theoretical curves, it is shown broadened by a $\Gamma = 0.5$ eV Lorentzian in the right panel, whereas the experimental $E2$ feature, displayed in the left panel, is best fitted with a pseudo-Voigt profile of approximately 2-eV width.

With the procedure described above, the data sets of all *R* compounds were successfully analyzed, and for each incident photon energy the integrated intensities of the main features could be determined. These separated sets of dipolar and quadrupolar integrated intensities yield the resonance energies of the $E1$ and $E2$ features, and more importantly, they provide the correct ratio of $E2$ to $E1$ transition strengths, since the $E1$ contribution to the $E2$ feature has been accurately subtracted. The results of the analysis are summarized in Fig. 6. For each $R_2Fe_{14}B$ system, we plot, as a function of the incident energy, the intensities obtained for the dipolar (○) and quadrupolar (□) contributions. The results are shown in arbitrary units. The intensities have been normalized in such a way that the dipolar scale (right side of each plot) has a maximum of unity. In order to render the quadrupolar contribution visible, the data are referred to different scales on the left and right sides of the plot, but in the same

arbitrary units. The experimental CFS scans of the dipolar features *B* (dotted thick line) are also shown in Fig. 6. They have been conveniently scaled to adjust the maximum intensities obtained from the fitting analysis of the IXS data. To guide the eye, profiles fitting the extracted quadrupolar intensities have also been incuded in the figure. The integrated intensity ascribed to dipolar transitions is the sum of *B* and *C* features. This is the reason for the ''absorption-edge-like'' shape of the resulting curve. The *B* and *C* intensities have not been independently presented because the strong dipolar resonance occurring at the whiteline incident energy has an important contribution from both *B* and *C* structures. These contributions are difficult to separate between the edge and the whiteline energies. The integral of the whole experimental curve is a value which can be determined with much better accuracy than the separate intensities of the *B* and *C* features.

As we pointed out already in our previous publication,[17] for Nd and Sm it has been necessary to fit the experimental data with two additional profiles below the dominating dipolar final-state feature. The analysis shows that the two features, labeled $A1$ and $A2$ and represented in Fig. 6 by black and white squares, respectively, resonate at slightly different energies. The peak intensities of these two structures coincide with a ''negative to positive'' double structure in the corresponding XMCD.[17] Both RIXS and XMCD structures can be interpreted within a simple one-electron picture: the $A1$ structure originated in the promotion of a core electron to a hole in the partially filled ''spin-up'' $4f$ subshell, giving rise to the $2p^5 4f^{(n+1)\uparrow} 5\tilde{d^n}$ intermediate state, i.e., to excited terms with total spin $\mathbf{S} = (n+1)/2$. Alternatively, the $A2$ feature corresponds to the $E2$ excitation to the fully empty ''spin-down'' $4f$ subshell, with a $2p^5 4f^{n\uparrow 1\downarrow} 5\tilde{d^n}$ intermediate state, and to excited terms with total spin $\mathbf{S} = (n-1)/2$. Due to the first Hund's rule, the $4f^{n+1}$ configuration related to the $A2$ feature is more energetic than that to the $A1$, and consequently has a higher-energy transfer in the RIXS spectra. The experimental energy separation between $A1$ and $A2$ features is in good agreement with the energy difference between the ground and the first excited terms for $4f^{n+1}$ configurations.[17,33,34] Recent calculations of the $E2$ $2p \rightarrow 4f$ XAS spectra[20] for Nd and Sm show as well the existence of a double-peak structure, compatible with our observation. Moreover, our model explains as well the change of sign of the $E2$ dichroic signal at the L_3 edges of light rare earths, a quite general fact observed in several systems. This interpretation is also in accord with a quantitative analysis of XRMS on $Nd_2Fe_{14}B$.[35] Moreover, Hague[36] independently confirmed the presence of the $A1$ and $A2$ structures in a RIXS study on Ce compounds.

The analysis for $Ho_2Fe_{14}B$ reveals another peculiarity. Despite the fact that in the RIXS spectra a second discrete feature at the low-energy-transfer side of the $E1$ feature can not be identified, the spectral decomposition leads to an intensity variation with two peaks. This high-energy $E2$ feature resonates $\approx 4 \pm 1$ eV below the dipolar resonance. This behavior was reproduced in calculations of the Ho^{3+} quadrupolar RIXS by van Veenendaal *et al.*,[6] where a second $E2$ contribution appears at about 3-eV larger energy transfer as the main $E2$ feature. A similar behavior, but less pronounced, is also observed for Tb and Dy, where the $E2$ intensity variation shows a small shoulder toward higher incident photon energies.

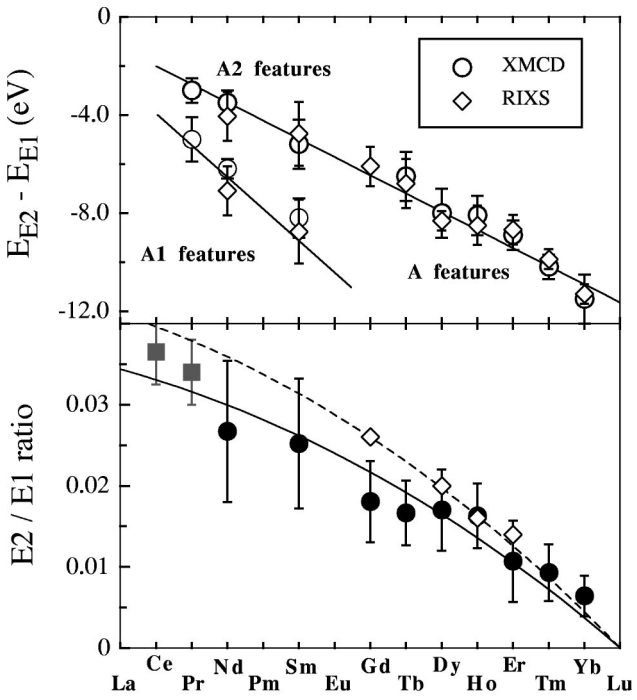

FIG. 7. Top panel: Energy separation $E_{E2}-E_{E1}$ between the quadrupolar and dipolar resonance energies, as derived from RIXS ($\diamond$) and XMCD ($\bigcirc$) as a function of the *R* element. Lines are guides to the eye. Bottom panel: Ratio of quadrupolar to dipolar transition strength obtained from the analysis described in the text as a function of the *R* element. The solid and dashed lines result from fitting the theoretical $E2/E1$ intensity evolution to our results ($\bullet$) and to values from Ref. 18 ($\diamond$), respectively. See text for more details.

In our previous paper[17] we performed a comparison between the position of the quadrupolar RIXS features with the XMCD spectra recorded on the same samples. The excellent agreement between the positions of diverse features found on RIXS and XMCD experiments strongly suggested the $E2$ origin of the L_3 dichroic pre-edge structures. This was posteriorly confirmed[30] in the case of $Nd_2Fe_{14}B$ by an analysis of the temperature and angular dependence of XMCD upon the spin reorientation transition that this compound undergoes at $T \approx 135$ K.

The quantitative results concerning the energy position and the relative strength of quadrupolar to dipolar excitation channel are summarized in Fig. 7. The top panel shows the separation between the resonance energies of the quadrupolar and dipolar features, $E_{E2}-E_{E1}$ ($\diamond$). For completeness, the energy position in the corresponding XMCD spectra of the $R_2Fe_{14}B$ compounds are displayed as well ($\bigcirc$). Features *A* and $A2$ in heavy and light *R*, respectively, follow the same trend as a function of the filling of the $4f$ shell. This is well understood with the proposed model as the photoelectron is excited to the same $4f$ subshell. The $E_{E2}-E_{E1}$ values and their evolution through the rare-earth series are in good

agreement with available theoretical results for R = Gd to Tm.[21]

In particular, the extracted value of $E_{E2}-E_{E1}=11.3\pm0.4$ eV for $Yb_{14}Fe_2B$ confirms the previously made prediction of $E_{E2}-E_{E1}=10.5\pm1.5$ eV, extrapolated from the observed trend along the rare-earth series.[17] Our results suggest that for $YbFe_2$ as well, the lowest-energy XMCD peak is of $E2$ character, as it appears at an incident energy ≈12 eV below the dipolar resonance. This is in disagreement with a previous analysis of temperature dependent XMCD spectra,[9] where the central feature at the Yb L_3 energy, 5 eV below the whiteline maximum was identified as a quadrupolar contribution. A similar (though less pronounced) hump was found by Chaboy *et al.*[37] in the XMCD at the Yb L_3 edge on $Yb_2Fe_{14}B$, whose energy position is also shown in Fig. 7.

The bottom panel of Fig. 7 shows the relative strength of the $E2$ channel compared to the $E1$ channel for the rare-earth series. The dipolar intensities have been obtained as the integral of the correctly scaled experimental CFS scans of features *B*. The $E2$ contributions were extracted by integration of the fitted Lorentzian profile. For Nd and Sm, the intensities of the two quadrupolar features were added. Despite the quite large error bars, a decreasing trend of the $E2/E1$ intensity ratio with increasing atomic number can be observed, ranging in this series from $E2/E1=0.027$ for Nd to 0.0065 for Yb. Qualitatively, this behavior can be easily understood: while the $E1$ intensity remains approximately constant along the series, one expects the $E2$ intensity to decrease as the number of unoccupied $4f$ states is reduced from Nd to Yb. As a matter of fact, the $E2/E1$ ratio is proportional to $(14-n)(Z\alpha)^2$ (where $\alpha=1/137$ is the fine structure constant and n the number of $4f$ electrons).[18] The solid line in the bottom panel of Fig. 7 represents the best fit to the data with the above functional dependence.

A decreasing trend of the quadrupolar to dipolar strength ratio was also obtained by Loeffen *et al.*, by deconvolution of high-quality absorption spectra[18] recorded at the L_3 edges of Gd, Dy, Ho, and Er in a group of five rare-earth insulators. Their results are plotted for comparison as well in the bottom panel of Fig. 7 ($\diamond$). The overall agreement between the results of two very different methods to obtain the $E2/E1$ ratios is very satisfying. The best fit of the $(14-n)(Z\alpha)^2$ dependence to the results from Ref. 18 is shown as a dashed line, evidencing a quantitative agreement with our results for Dy, Ho, Er, Tm, and Yb. For Gd, Tb, Sm, and Nd, we find slightly lower $E2/E1$ values, although $E2/E1=0.018$ for Gd is coincident with the value previously found[15] in the insulating garnet $Gd_3Ga_5O_{12}$. These slight differences would be related to the fact that as one approaches the light rare earths the energy difference between quadrupolar $A2$ and dipolar *B* features decreases, thus making a proper separation difficult. This is evidenced for Dy in Fig. 4 by the imposibility of separately observing the predicted feature labeled *e*, and consequently, of computing its contribution. The increase of the error bars for light rare earths is also related to this systematic error.

The general agreement between the results from different experiments and data analysis allow us to make a prediction for the $E2/E1$ ratio to be found in Ce and Pr compounds: the data and fits shown in Fig. 7 lead to a range of values of $E2/E1=0.037\pm0.008$ and 0.034 ± 0.008 for Ce and Pr, respectively. These ratios should arise from integration of $A1$ and $A2$ features, whose energies with respect to the dipolar resonance can be obtained by inspection of the top panel of Fig. 7.

V. CONCLUSION

We have presented a systematic resonant inelastic x-ray scattering study at the L_3 absorption edge of rare-earth ions in the $R_2Fe_{14}B$ series of intermetallic magnetic materials. A decomposition of each individual IXS spectrum has been performed by fitting pseudo-Voigt functions to the dominating dipolar contribution, and obtaining the quadrupolar ones by subtraction. This procedure allowed us to determine the intensity evolution of $E1$ and $E2$ features as a function of incident photon energy, resulting in the determination of both their resonance energies and their relative strengths. The quadrupolar origin of the observed pre-edge features is supported by the agreement with the quadrupolar RIXS spectra calculated by different authors. We want to stress that the $E2/E1$ intensity ratio obtained from RIXS experiments provides the partial $E1$ and $E2$ absorption cross sections, as the integrated intensity of the inelastic x-ray scattering spectrum at a given incident energy, and that it is proportional to the absorption cross section at this energy.[31]

This work gives a set of experimental test values for the intensity of quadrupolar excitation channels with respect to the dipolar ones in metallic systems, which should be useful in the validation of combined band theory–atomic multiplet calculations intending a theoretical description of the core-hole spectroscopies (especially magnetic ones) at the $L_{2,3}$ absorption edges of rare-earth ions, as well as allowing the proper use of the magneto-optical sum rules at the hybridized $5d$ orbitals of rare-earth ions in intermetallic systems.

ACKNOWLEDGMENTS

We wish to thank the staffs of the European Synchrotron Radiation Facility and the National Synchrotron Light Source for their assistance during the experiments. F. Sette and C. C. Kao are specially acknowledged for the design and construction of the ESRF ID16 and NSLS X21 beamlines, respectively, and their valuable help during the experiments. J. Chaboy is acknowledged for fruitful discussions and for providing the samples used in the experiments. We thank L. Sève for useful discussions and support. F.B. acknowledges the European Commission, which partially financed this work through a Marie Curie grant, and a CAI-DGA Europa grant.

[1] G. Schütz, M. Knülle, R. Wienke, W. Wilhelm, W. Wagner, P. Kienle, and R. Frahm, Z. Phys. B **73**, 67 (1988).
[2] P. Fischer, G. Schütz, S. Stähler, and G. Wiesinger, J. Appl. Phys. **69**, 6144 (1991).
[3] F. Baudelet, C. Giorgetti, S. Pizzini, C. Brouder, E. Dartyge, A. Fontaine, J. P. Kappler, and G. Krill,J. Electron Spectrosc. Relat. Phenom. **62**, 153 (1993).
[4] D. Gibbs, D. R. Harshman, E. D. Isaacs, D. B. McWhan, D. Mills, and C. Vettier, Phys. Rev. Lett. **61**, 1241 (1988).
[5] P. Carra and M. Altarelli, Phys. Rev. Lett. **64**, 1286 (1990).
[6] M. van Veenendaal, J. B. Goedkoop, and B. T. Thole, Phys. Rev. Lett. **78**, 1162 (1997).
[7] B. N. Harmon and A. J. Freeman, Phys. Rev. B **10**, 1979 (1974).
[8] J. C. Lang, G. Srajer, C. Detlefs, A. I. Goldman, H. König, X. Wang, B. N. Harmon, and R. W. McCallum, Phys. Rev. Lett. **74**, 4935 (1995).
[9] C. Giorgetti, E. Dartyge, C. Brouder, F. Baudelet, C. Meyer, S. Pizzini, A. Fontaine, and R. M. Galera, Phys. Rev. Lett. **75**, 3186 (1995).
[10] G. Helgesen, J. P. Hill, T. R. Thurston, D. Gibbs, J. Kwo, and M. Hong, Phys. Rev. B **50**, 2990 (1994).
[11] C. Detlefs, A. H. M. Z. Islam, A. I. Goldman, C. Stassis, P. C. Canfield, J. P. Hill, and D. Gibbs, Phys. Rev. B **55**, R680 (1997).
[12] A. Koizumi, H. Maruyama, K. Namikawa, K. Mori, H. Kawata, M. Ando, and H. Yamazaki, J. Phys. Soc. Jpn. **61**, 399 (1992).
[13] F. Bartolomé, J. M. Tonnerre, D. Raoux, J. Chaboy, L. M. García, J. Bartolomé, H. Maruyama, A. Marcelli, F. Rieutord, and R. Simon, J. Phys. IV **7**, C2-437 (1997).
[14] K. Hämäläinen, D. P. Siddons, J. B. Hastings, and L. E. Berman, Phys. Rev. Lett. **67**, 2850 (1991).
[15] M. H. Krisch, C. C. Kao, F. Sette, W. A. Caliebe, K. Hämäläinen, and J. B. Hastings, Phys. Rev. Lett. **74**, 4931 (1995).
[16] M. H. Krisch, F. Sette, U. Bergmann, C. Masciovecchio, R. Verbeni, J. Goulon, W. Caliebe, and C. C. Kao, Phys. Rev. B **54**, R12 673 (1996).
[17] F. Bartolomé, J. M. Tonnerre, L. Sève, D. Raoux, J. Chaboy, L. M. García, M. Krisch, and C. C. Kao, Phys. Rev. Lett. **79**, 3775 (1997).
[18] P. W. Loeffen, R. F. Pettifer, S. Müllender, M. A. van Veenendaal, J. Röhler, and D. S. Silvia, Phys. Rev. B **54**, 14 877 (1996).
[19] S. Tanaka, K. Okada, and A. Kotani, J. Phys. Soc. Jpn. **63**, 2780 (1994).
[20] M. van Veenendaal and R. Benoist, Phys. Rev. B **58**, 3741 (1998).
[21] X. Wang, T. C. Leung, B. N. Harmon and P. Carra, Phys. Rev. B **47**, 9087 (1993).
[22] C. J. Sparks, Phys. Rev. Lett. **33**, 262 (1974).
[23] P. Eisenberger, P. M. Platzman, and H. Winick, Phys. Rev. B **13**, 2377 (1976).
[24] P. L. Cowan, *Resonant X-Ray Raman Scattering From Atoms and Molecules* in *Resonant Anomalous X-Ray Scattering. Theory and Applications*, edited by G. Materlik, C. J. Sparks, and K. Fischer (Elsevier, Amsterdam, 1994).
[25] P. Carra, M. Fabrizio, and B. T. Thole, Phys. Rev. Lett. **74**, 3700 (1995).
[26] L. Nordström, B. Johansson, and M. S. S. Brooks, J. Phys.: Condens. Matter **5**, 7859 (1993).
[27] F. Sette *et al.* (unpublished).
[28] C. C. Kao, K. Hämäläinen, M. Krisch, D. P. Siddons, T. Oversluizen, and J. B. Hastings, Rev. Sci. Instrum. **66**, 1699 (1995).
[29] J. Chaboy, L. M. García, F. Bartolomé, H. Maruyama, A. Marcelli, and L. Bozukov, Phys. Rev. B **57**, 13 386 (1998).
[30] J. Chaboy, F. Bartolomé, L. M. García, and G. Cibin, Phys. Rev. B **57**, R5598 (1998).
[31] M. van Veenendaal, P. Carra, and T. Thole, Phys. Rev. B **54**, 16 010 (1996).
[32] J. Goedkoop, Ph.D. thesis, University of Nijmegen, 1989.
[33] S. Hüfner, Z. Phys. **165**, 396 (1961).
[34] L. G. DeShazer and G. H. Dieke, J. Chem. Phys. **38**, 2190 (1963).
[35] F. Bartolomé, J. M. Tonnerre, L. Sève, D. Raoux, J. E. Lorenzo, J. Chaboy, L. M. Garca, J. Bartolomé, M. Krisch, A. Rogalev, R. Serimaa, C. C. Kao, G. Cibin, and A. Marcelli, J. Appl. Phys. **83**, 7091 (1998).
[36] C. F. Hague (unpublished).
[37] J. Chaboy, L. M. García, F. Bartolomé, J. Bartolomé, H. Maruyama, K. Kobayashi, N. Kawamura, A. Marcelli, and L. Bozukov, J. Phys. IV **7**, C2-449 (1997).